Broadband subwavelength near-field imaging in terahertz range by a two-dimensional rhombic-lattice photonic crystal

Z. H. WU[a,*], J. X. LIU[b], Q. LUO[a], X. WEN[a]
[a]School of Sciences, Southwest Petroleum University, 610500, Chengdu, China
[b]Science and Technology on Electronic Information Control Laboratory, 610036, Chengdu, China

In this paper, an original realization of broadband subwavelength terahertz near-field imaging is achieved by using a two-dimensional rhombic-lattice photonic crystal. The evanescent modes of a source are canalized by the Bloch modes of the photonic crystal that served as the flat lens. The structure is optimal designed by analyzing the equal frequency contours of the photonic crystal with the plane wave expansion method. The bandwidth of the central frequency for subwavelength imaging is 17.42% that covers frequencies from 2.373 THz to 2.826 THz. The subwavelength imaging is demonstrated by means of finite-difference time-domain method.

1. Introduction

Terahertz (THz) technologies have attracted more and more interests and studies from all over the world because of the potential applications in many scientific fields. The applications of THz waves have been exploited intensively in many fields, such as THz spectroscopy, imaging, screening, sensing, antenna, and so on [1-4]. To manipulate the THz waves in an integrated circuit is required for these applications. Recently, Photonic crystals (PhCs) are reported to be promising materials in the THz devices design for their non-loss, low dispersion and transparency in the THz band [5, 6].

PhCs are artificial periodic dielectric structures and are considered as the most promising structures to realize compact and highly functional photonic integrated circuits. Lots of optical devices based on PhCs have been designed, such as resonators [7], filters [8], optical switches [9], beam splitters [10], and fibers [11]. In this paper, we suggest a new PhC structure to realize the broadband subwavelength imaging for THz waves.

The resolution of imaging systems with conventional lenses is restricted by the diffraction limit. Light will be fully diffracted in all directions when transmitting through a subwavelength aperture. A great progress for subwavelength imaging had been made by Pendry in 2000. A "perfect lens" made with left-handed materials (LHM), which is characterized by simultaneous negative permittivity and permeability, is proposed by Pendry to show that the negative refraction in such materials can overcome the diffraction limit [12, 13].

In recent years, with the rising studies on photonic crystals (PhCs), it is found that the negative refraction can also be realized in PhCs, which have both positive permittivity and permeability [14, 15]. This finding provides a new approach to achieve subwavelength imaging. As a new emerging research field, the focus and imaging properties of electromagnetic waves by two-dimensional (2D) PhC flat lenses have been intensively studied theoretically and experimentally. Notomi *et al.* have proved the negative refraction in PhCs is possible in theory [14, 16]. Luo *et al.* reported the negative refraction behaviors and the imaging properties of a point source in a square array PhC in near field [17]. And in the same year, they realized the negative refractions in a three-dimensional PhC. Feng *et al.* have studied the subwavelength imaging properties both in square-lattice and triangular-lattice PhC slabs [18]. Roy *et al.* focused the transmitted light into subwavelength hot spots by using a planar plasmonic metamaterial with spatially variable meta-atom parameters [19]. Cubukcu *et al.* verified the subwavelength imaging in the microwave band experimentally [20]. Jiang *et al.* realized all-angle negative refraction and far-field imaging effects via 2D all-solid PhCs [21]. Ma *et al.* proposed a new 2D PhC structure consisting of periodic array air holes in silicon to make the light radiating from a point source can form a subwavelength imaging through a wedge PhC [22].

Most of these schemes are based on the negative refraction properties of PhCs. However, it is also pointed out that the self-collimation in PhCs can also lead to the subwavelength imaging [23]. The self-collimation is an unusual dispersion property in PhCs. It provides a brand new way of confining the light propagation besides the conventional PC waveguide. Lots of optical devices have been proposed based on the self-collimation effect in recent years. There are also some studies focus on the imaging properties by the self-collimation effect in PhCs. Feng *et al.*

and Li *et al.* have discussed the subwavelength imaging by self-collimation effect in PhCs with elliptical, rectangular cylinders and wavy structure, respectively [24-26].

The subwavelength imaging performances are generally influenced by the light incident angle, whether the image is formed by negative refraction effect or self-collimation effect. The bandwidth for imaging are usually very narrow. To overcome these disadvantages, in this paper, we bring a new realization of broadband near-field subwavelength imaging for THz waves by a rhombic-lattice PhC.
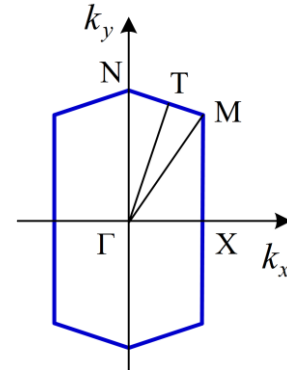
2. Theory and structure

Light propagation in a PhC structure is governed by its dispersion surfaces. The group velocity v_g is given by the relationship [27]

$$v_g = \nabla_k \omega(k)$$

$$= e_x \cdot \frac{\partial}{\partial k_x} \omega(k_x, k_y, k_z) + e_y \cdot \frac{\partial}{\partial k_y} \omega(k_x, k_y, k_z)$$

$$+ e_z \cdot \frac{\partial}{\partial k_z} \omega(k_x, k_y, k_z)$$
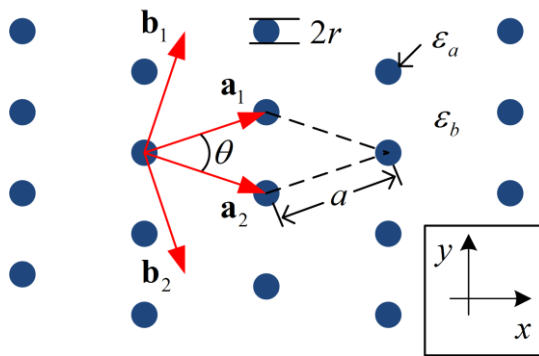
(a) geometry of the rhombic lattice   *(b) Illustration of the FBZ*
Fig. 1. (a) The geometry of the rhombic lattice and (b) its Illustration of the FBZ (color online)

The structure of the rhombic-lattice PhC consists of dielectric rods with permittivity of ε_a scatter in a uniform background medium with permittivity of ε_b as shown in fig. 1(a) [28, 29]. In this paper, we consider a 2D PhC structure with silicon rods arranged in a rhombic lattice in air. For the low absorbance in THz regime and mature processing technology, silicon is chosen as the material in our design. The acute angle θ contained by the two sides of the rhombus is defined as the lattice angle, which is defined in the range of $0° < \theta \leq 90°$. the side length a is defined as the lattice constant. To avoid the overlaps of the adjacent rods, the radius of the rods is confined to $r \leq a \sin(\theta/2)$ when $\theta \in (0°, 60°]$ and $r \leq 0.5a$ when $\theta \in [60°, 90°]$. Fig. 1(b) illustrates the first Brillouin zone (FBZ) of the rhombic lattice [28]. Γ, X, M, T, and N represent the special symmetry points. (a_1, a_2) and (b_1, b_2) represent the

where ω is the frequency at the wavevector k. Incident light propagates in directions normal to the dispersion surfaces and perpendicular to the equi-freqneucy contours (EFCs). The self-collimating phenomenon occurs where the EFC corresponding to a frequency is flat. The EFCs can be obtained by the plane wave expansion (PWE) method, which is frequently used to solve the eigenvalue problem of the Maxwell's equations.

The self-collimating imaging means that the light beam propagates in a PhC with no diffraction and converges to an image in another side of the PhC. The spatial variation of the spectral transfer to the Eigen modes which contain all the near-field details and all the details should be revealed in the image. We have reported the broadband all-angle self-collimation in a rhombic-lattice PhC [28]. Such a structure can also be used to realize the broadband subwavelength imaging.

primitive lattice vectors and the primitive reciprocal lattice vectors.

The boundary of the FBZ is determined by the k points at X, M, and N which can be deduced as [28, 29]:

$$k_X = (\frac{\pi}{a} \sec \frac{\theta}{2}, 0),$$

$$k_M = (\frac{\pi}{a} \sec \frac{\theta}{2} - \frac{\pi}{2a}(\csc \frac{\theta}{2} - \tan \frac{\theta}{2}),$$

$$k_N = (0, \frac{\pi}{2a} \frac{\sec^2 \frac{\theta}{2} + \csc^2 \frac{\theta}{2}}{\csc \frac{\theta}{2}}).$$

The eigen-frequencies at all k points in the FBZ can be calculated with the PWE method and the EFCs can be

obtained. By analyzing the EFCs, the self-collimating frequencies can be confirmed.

3. Broadband subwavelength Imaging

To achieve broadband subwavelength imaging, a parameter sweep technique is applied in the calculations. The EFCs for different lattice angles and radii of the rods is calculated by using PWE method. By analyzing the EFCs, it is found that the largest bandwidth for all-angle self-collimation is obtained when the lattice angle is $\theta=32°$ and the radius of the rods is $r=0.25a$ (15.23 μm), where $a=60.93$ μm is the lattice constant. Fig. 2 shows the corresponding EFCs of TM mode in the third band [29].

It is found that the EFCs is flat and open in the frequency range from $0.475c/a$ (2.339 THz) to $0.574c/a$ (2.826 THz), where c is the speed of light in vacuum. Moreover, the operation of all-angle self-collimation is confirmed by finite-difference time-domain (FDTD) method in frequency region from $0.482c/a$ (2.373THz) to $0.574c/a$ (2.826 THz), with a relative bandwidth of about 17.42% [29]. It indicates that the broadband subwavelength imaging is possible in this frequency range.
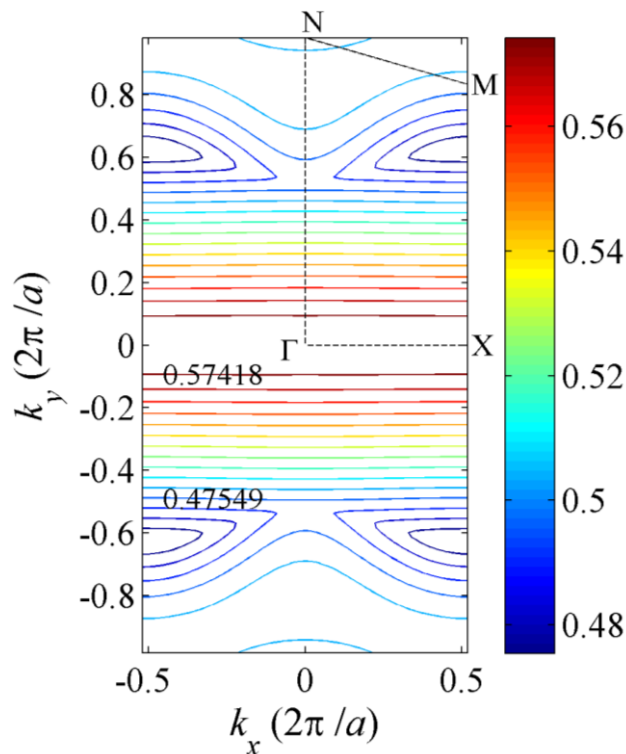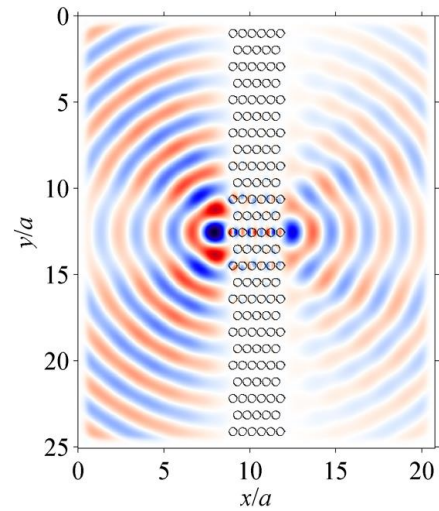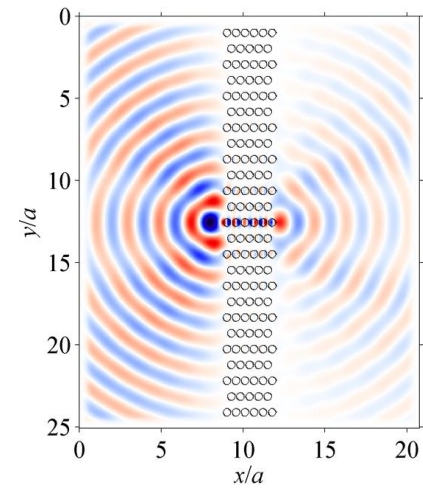

Fig. 2. The third band EFCs of TM mode
($\theta=32°$ and $r=0.25a$) (color online)

(a) f=0.490c/a (2.413 THz)

(b) f=0.530c/a (2.806 THz)
Fig. 3. Steady-state field distributions of the E_z
component for frequencies (a) f=0.490c/a (2.413 THz)
and (b) f=0.570c/a (2.806 THz) (color online)

Numerical simulations using the FDTD method to demonstrate the imaging performance of the PhC were performed. We consider a PhC slab consists of 25×11 silicon rods with $r=0.25a$ (15.23 μm) arranged in a rhombic lattice in air with lattice angle $\theta=32°$. THz waves with frequencies $f=0.490c/a$ (2.413 THz) and $f=0.570c/a$ (2.806 THz) are chosen in the simulations. An E_z-polarized point source is placed at the center of the y-direction and at a very close distance of $0.6a$ (36.56 μm) away from the left hand side of the PhC-air interface. The FDTD simulations of steady-state field distributions of the E_z component with frequency $f=0.490c/a$ (2.413 THz) and $f=0.570c/a$ (2.806 THz) are shown in Fig. 3(a) and 3(b), respectively. It can be seen clearly that the THz wave transmits through the PhC as a collimated beam and converges into a point image at the output port. The image is about $0.55a$ (33.51 μm) away from the right hand side of the PhC. The THz source and image are both very close to the PhC. It's a typical near-field imaging phenomenon.

Fig. 4 shows the normalized intensity in y-direction for frequencies $f=0.490c/a$ (2.413 THz) and $f=0.570c/a$ (2.806

THz). It's obvious that the main peak is far taller than the sub-peak. The half-width of the main peak is 0.930a（0.456λ）and 0.793a（0.419λ）for frequencies f=0.490c/a (2.413 THz) and f=0.570c/a (2.806 THz), respectively. It's

both smaller than the diffraction limit. Therefore, it reaches the resolution of subwavelength imaging.
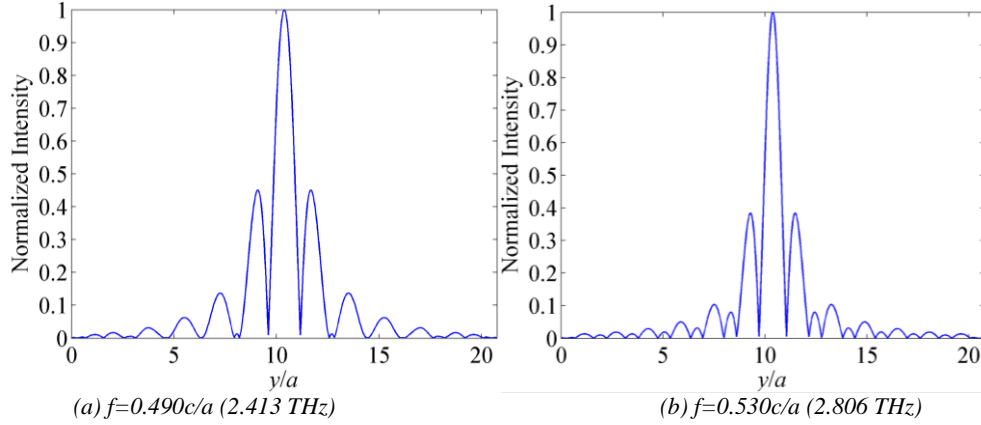

(a) f=0.490c/a (2.413 THz)   *(b) f=0.530c/a (2.806 THz)*

Fig. 4. Normalized intensity in y-direction for frequencies (a) f=0.490c/a (2.413 THz) and (b) f=0.570c/a (2.806 THz) (color online)

The imaging performance is influenced by the source position. Fig. 5(a), (b), (c), (d), (e), (f) show the steady-state field distributions of the E_z component for frequency f=0.490c/a (2.413 THz) when the light source is 0.40a, 0.60a, 0.80a, 1.00a, 1.50a and 2.00a away from the

left hand side of the PhC, respectively. The images are very clear when the distance is smaller than or equal to 0.80a. But it becomes a little vague when the distance is 1.00a and indistinguishable when that is 1.50a.

(a) d=0.40a   *(b) d=0.60a*   *(c) d=0.80a*

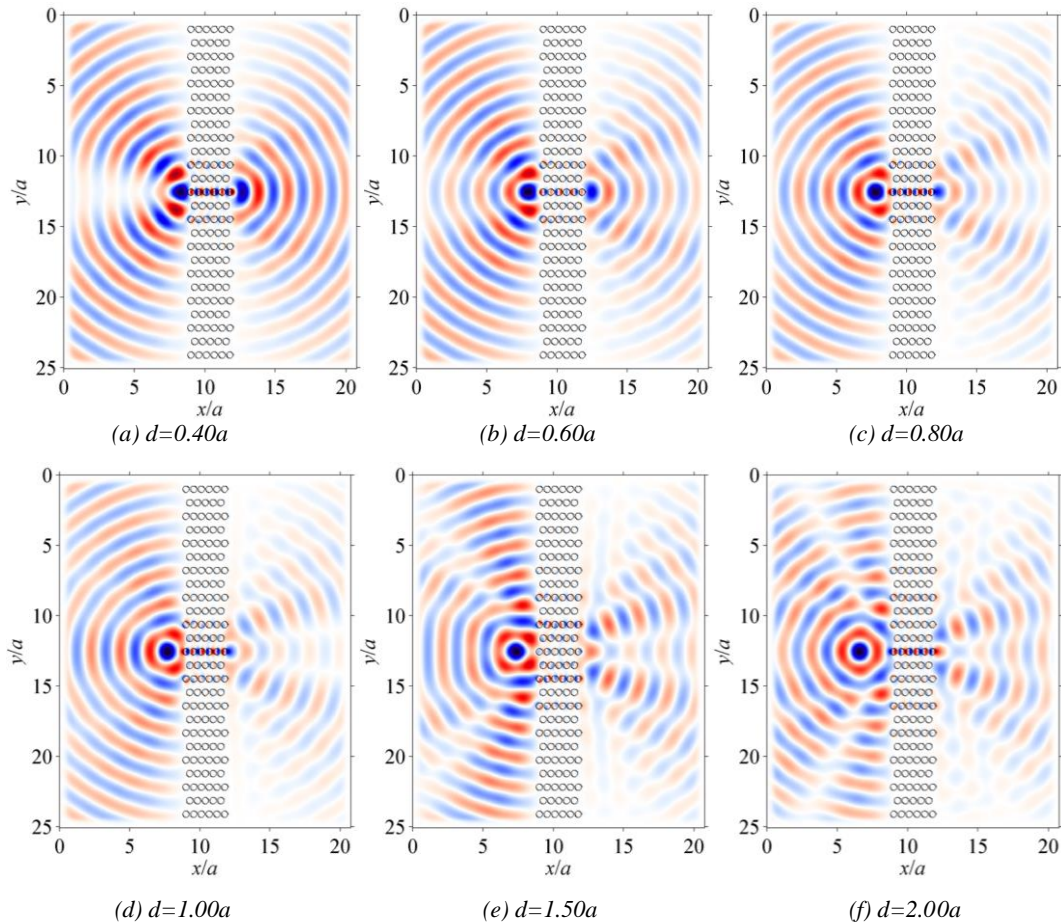*(d) d=1.00a*   *(e) d=1.50a*   *(f) d=2.00a*

Fig. 5. Steady-state field distributions of the E_z component with different distances of the light source (color online)
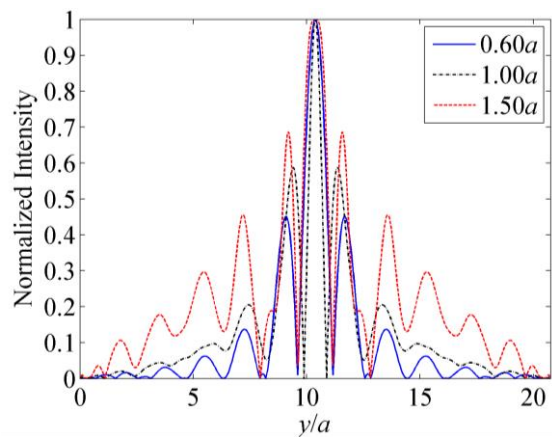
Fig. 6. Normalized intensity in y-direction of the images with different source distances (color online)

The normalized intensities in *y*-direction of the images with source distances 0.60a, 1.00a and 1.50a are shown in

Fig. 6 as the blue full line, black dashed line and red dotted line, respectively. It can be observed that the height of the sub-peaks increases with the source distance, and the main peak sinks into oblivion so that the image becomes indistinguishable. The results give the facts that the self-collimating imaging can only be achieved in near-field. This is different from the imaging by negative refraction. Another distinction is that the image by self-collimation is almost at the same position and invariant with the source distance, while it is changing by negative refraction.

The impact of the rod columns of the PhC on the imaging performance is also studied. The Steady-state field distributions of the E_z component with 7, 11 and 16 rod columns of the PhC is presented in Fig. 7. The simulations show that the image can be formed at the same position in any cases of rod columns. However, with the increases of the rod columns, the light intensity of the image is decreasing.

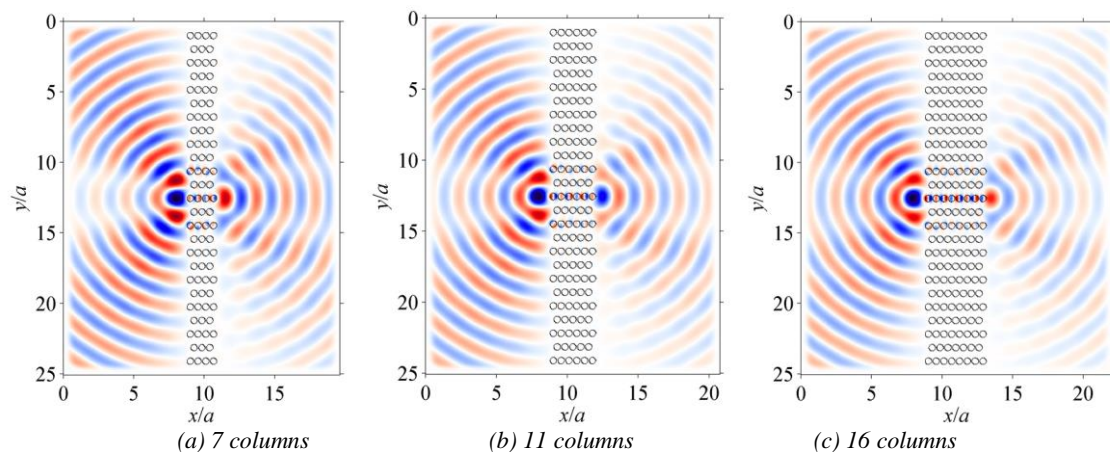*(a) 7 columns*   *(b) 11 columns*   *(c) 16 columns*

Fig. 7. Steady-state field distributions of the E_z component with different columns of the PhC (color online)

4. Conclusions

In summary, we report an original realization of broadband subwavelength near-field imaging for terahertz waves by using a rhombic-lattice PhC. The subwavelength imaging with a broad bandwidth of 17.42% is verified by numerical calculations. FDTD simulations are performed to demonstrate that the subwavelength imaging for terahertz waves in a broad frequency range from 0.482c/a (2.373THz) to 0.574*c/a* (2.826 THz) is achievable in the near-field. The subwavelength imaging by self-collimation is clearly different from that by negative refraction in PhCs. The image can be formed only when the source is in the near-field region. When the source is moved beyond the near-field space domain, the imaging effect strongly degrades. The image is always located in the near-filed region also, and has nothing with the source position nor the rod columns of the PhC. It is hopeful that these works may be helpful to the imaging applications of THz waves.

References

[1] J. R. Knab, A. J. L. Adam, R. Chakkittakandy, P. C. M. Planken, Appl. Phys. Lett. **97**(3), 0311151 (2010).
[2] L. Minkevicius, D. Jokubauskis, I. Kasalynas, S. Orlov, A. Urbas, G. Valusis, Opt. Express **27**(25), 36358 (2019).
[3] K. Ahmed, F. Ahmed, S. Roy, B. K. Paul, M. N. Aktar, D. Vigneswaran, M. S. Islam, IEEE Sens. J. **19**(9), 3368 (2019).

[4] A. Elakkiya, S. Radha, B. S. Sreeja, E. Manikandan, J. Optoelectron. Adv. M. **20**(9-10), 474 (2018).

[5] H. Liu, J. Yao, D. Xu, P. Wang, Appl. Phys. B-Lasers **87**(1), 57 (2007).

[6] Z. H. Wu, B. Tang, Q. Zhang, Y. Qiu, Optik **124**(17), 2844 (2013).

[7] F. Metehri, M. Y. Mahmoud, G. Bassou, J. Optoelectron. Adv. M. **21**(5-6), 289 (2019).

[8] R. Talebzadeh, M. Soroosh, J. Optoelectron. Adv. M. **17**(11-12), 1593 (2015).

[9] Z. Wu, B. Tang, Q. Zhang, Q. Luo, Y. Qiu, Z. Liu, F. Wang, J. Optoelectron. Adv. M. **18**(9-10), 745 (2016).

[10] R. Arunkumar, J. K. Jayabarathan, S. Robinson, J. Optoelectron. Adv. M. **21**(7-8), 435 (2019).

[11] J. Broeng, D. Mogilevstev, S. E. Barkou, A. Bjarklev, Opt. Fiber Technol. **5**(3), 305 (1999).

[12] V. G. Veselago, Physics-Uspekhi **10**(4), 509 (1968).

[13] J. B. Pendry, Phys. Rev. Lett. **85**(18), 3966 (2000).

[14] M. Notomi, Phys. Rev. B. **62**(16), 10696 (2000).

[15] T. Baba, T. Matsumoto, T. Asatsuma, Smart Optics **55**, 91 (2009).

[16] M. Notomi, Physics and Simulation of Optoelectronic Devices **IX**(4283), 428 (2001).

[17] C. Luo, S. G. Johnson, J. Joannopoulos, J. Pendry, Phys. Rev. B **65**(20), 201104 (2002).

[18] S. Feng, Y. X. Li, B. Lei, J. Y. Hu, Y. Q. Wang, W. Z. Wang, Solid State Commun. **152**(11), 929 (2012).

[19] T. Roy, E. T. F. Rogers, N. I. Zheludev, Opt. Express **21**(6), 7577 (2013).

[20] E. Cubukcu, K. Aydin, E. Ozbay, S. Foteinopoulou, C. M. Soukoulis, Phys. Rev. Lett. **91**(20), 207401 (2003).

[21] L. Y. Jiang, H. Wu, X. Y. Li, Opt. Commun. **285**(9), 2462 (2012).

[22] H. L. Ma, B. M. Liang, S. L. Zhuang, J. K. Niu, J. B. Chen, Opt. Lett. **42**(19), 4012 (2017).

[23] Z. Y. Li, L. L. Lin, Phys. Rev. B **68**(24), 245110 (2003).

[24] S. Feng, Z. Y. Li, Z. F. Feng, K. Ren, B. Y. Cheng, D. Z. Zhang, J. Appl. Phys. **98**(6), 063102 (2005).

[25] S. Feng, Z. Y. Li, Z. F. Feng, B. Y. Cheng, D. Z. Zhang, Phys. Rev. B **72**(7), 075101 (2005).

[26] Y. Li, P. Gu, J. Zhang, M. Li, X. Liu, Appl. Phys. Lett. **88**(15), 151911 (2006).

[27] D. W. Prather, S. Y. Shi, J. Murakowski, G. J. Schneider, A. Sharkawy, C. H. Chen, B. L. Miao, R. Martin, J. Phys. D Appl. Phys. **40**(9), 2635 (2007).

[28] Z. Wu, K. Xie, H. Yang, P. Jiang, X. J. He, J. Optics-Uk **14**(1), 015002 (2012).

[29] Z. H. Wu, K. Xie, H. J. Yang, Optik **123**(6), 534 (2012).

_____

[*]Corresponding author: wuzhenhai@swpu.edu.cn